

Laser nitriding of the surface of phosphor bronze

B. S. Yilbas · S. S. Akhtar · C. Karatas

Received: 3 March 2010 / Accepted: 5 June 2012 / Published online: 26 June 2012
© Springer-Verlag London Limited 2012

Abstract Phosphorous bronze finds applications in industry because of its resistance to fatigue and ease of heat dissipation due to its high thermal conductivity. Laser treatment of bronze surface improves the hardness of the surface through forming a dense layer in the surface region. Consequently, in the present study, laser treatment of a bronze surface is investigated. Thermal stress and temperature fields developed during the laser-treated region are modeled after considering the transient three-dimensional situation in line with the experimental conditions. An experiment is carried out, and the resulting surfaces treated by a laser beam are characterized using scanning electron microscope, energy dispersive spectroscopy, and X-ray diffraction. It is found that high rate of strain developed in the heated region, due to fast-cooling rates, results in high von Mises stress in the surface region. The laser-treated region is free from cracks, and surface hardness increases almost four times above the base material hardness after the laser treatment process.

Keywords Laser · Bronze · Thermal stress · Temperature

1 Introduction

Phosphorous bronze alloys are widely used in industry due to their resistance to fatigue and chemical corrosion. One of

the uses of phosphorus bronze is in bearing applications due to its low friction coefficient. Although it is used as a bearing surface, low surface hardness limits its applications. The hardness of the alloy can be improved through surface treatment techniques. One of the effective techniques is the laser gas-assisted processing of the alloy surface. Although thermal conductivity of the alloy is high, high power intensity of laser can be used to melt the surface at a required depth. Moreover, laser processing has many advantages over the conventional techniques, and some of these advantages include local treatment, precision of operation, fast processing time, and low processing cost. In laser gas-assisted processing, nitrogen gas is used during the melting of the alloy surface. This, in turn, generates a nitrided surface and dense structures, which is expected to improve the surface hardness of the alloy. Consequently, investigation into laser gas-assisted nitriding of phosphorous bronze becomes essential.

Considerable research studies were carried out for laser treatment and nitriding of copper alloy surfaces. The laser melting of copper alloy and the structural analysis was carried out by Vanderberg and Draper [1]. They showed that laser surface melting of conventionally cast aluminum bronze resulted in the formation of several metastable phases. The cavitation erosion of laser-quenched aluminum bronze was investigated by Gabriel et al. [2]. They indicated that laser-treated alloy had better cavitation erosion resistance than that of the untreated alloy. The copper-nitrided and tin nitride films were examined by Maruyama and Marishita [3]. They showed that some of the tin formed during the thermal decomposition was observed to coalesce into a thick layer leaving areas where constrictions were evident. This occurred due to the relatively low melting point of tin. Formation of nitride phases in the course

B. S. Yilbas (✉) · S. S. Akhtar
ME Department, KFUPM,
Dhahran 31261, Saudi Arabia
e-mail: bsyilbas@kfupm.edu.sa

C. Karatas
Engineering College,
Hacettepe University,
Ankara, Turkey

of nitrogen implantation into copper and its alloys was investigated by Zukowshi et al. [4]. They indicated that the large rate of diffusion of nitrogen ions in the substrate surface was due to the presence of radiation-enhanced diffusion during implantation. The thin film deposition of copper nitride was studied by Wang et al. [5]. They showed that in pure nitrogen atmosphere, the flux of nitrogen had little influence on the copper nitride structure. The structure and properties of copper nitride films were examined by Pierson [6]. He indicated that incorporation of nitrogen in copper-based coating resulted in an abrupt increase of microhardness and high values of nitrogen flow rates. The growth of structural and optical properties of copper nitride films were investigated by Borsew and Boerms [7]. They showed that as a pure phase, the behavior of a grown film was typical for an insulator with a large optical gap. However, if low amount of copper impurities were present in the copper nitride, the film had the overall behavior of an insulator with reduced optical band gap. The cavitation erosion resistance of a copper-based alloy treated by a laser surface-melting process was investigated by Tang et al. [8]. They indicated that the laser surface-melted samples exhibited grain refinement, and the damaged surface of laser-treated samples showed brittle fracture facets. The properties of copper nitride thin films were examined by Yue et al. [9]. They showed that the grain size of thin films could become small when the N_2 ratio increased, and Cu_3N phase could completely decompose into Cu and N_2 through vacuum-annealing treatment. The surface characterization of nitride structures on copper was carried out by Cristina et al. [10]. They showed that nitrogen-binding energy shifted nonmonotonically along the whole process indicating that the N–Cu bonding was dependent on the atomic arrangement and on the amount of nitrogen.

Thermal stress analysis for laser treatment of tool steel surface was carried out previously [11]; however, the differences in thermal and mechanical properties between phosphorous bronze and tool steel result in different temperature and thermal stress fields in the substrate materials. Moreover, the experience gained from the previous model study [11] is useful to comprehend the simulation of temperature and stress fields for phosphorous bronze. In the present study, laser gas-assisted melting of phosphorous bronze at nitrogen gas environment is carried out. Temperature and stress fields during the laser processing are predicted in line with the experimental conditions. The microstructural and morphological changes in the laser-irradiated region are examined using scanning electron microscope (SEM), energy dispersive spectroscopy (EDS), and X-ray diffraction (XRD). The microhardness of the laser-treated surface is measured.

2 Experimental

The CO_2 laser (LC-ALPHAIII) delivering nominal output power of 2 kW was used to irradiate the workpiece surface [12]. The nominal focal length of the focusing lens of 127 mm was employed. The laser beam diameter focused at the workpiece surface was on the order of 0.9 mm. Nitrogen-assisting gas emerging from the conical nozzle and coaxially with the laser beam will be used. Laser surface treatment process was carried out at different laser parameters. It should be noted that increasing laser output power beyond 80 W resulted in high surface roughness due to melt flow during over-melting of the surface and surface cracks due to high temperature gradients as well as nitride species formed at the surface vicinity. Alternatively, reducing the laser power below 80 W lowered the depth of laser-treated layer. In addition, reducing laser scanning speed below 10 cm/s increased the surface roughness due to over-melting of the surface, while increasing its value reduced the laser treatment depth. Consequently, laser parameters resulting in crack-free surfaces with low surface roughness were selected. Laser treatment conditions are given in Table 1. The phosphorous bronze of 3 mm in thickness and $20 \times 10 \text{ mm}^2$ (length \times width) samples are used in the experiments. The chemical composition of the bronze is given in Table 2.

Material characterization of the laser-nitrided surfaces was carried out using SEM and XRD. Jeol 6460 electron microscopy is used for SEM examinations, and Bruker D8 Advanced having $CuK\alpha$ radiation is used for XRD analysis. A typical setting of XRD was 40 kV and 30 mA and scanning angle (2θ) range of $20\text{--}80^\circ$. A Microphotronics digital microhardness tester (MP-100TC) was used to obtain microhardness at the surface of the nitride layer. The standard test method for Vickers indentation hardness of advanced ceramics (ASTM C1327-99) was adopted. Microhardness was measured at the workpiece surface after the laser treatment process. The measurements were repeated five times at each location for the consistency of the results. It should be noted that laser-treated layer extends almost $50 \mu\text{m}$ below the surface, and nitride diffusion depth is on the order of $30 \mu\text{m}$ in the treated layer. Therefore, microhardness measurement across laser-treated depth is omitted due to low resolution and the precision limits.

2.1 Residual stress measurement

The position of the X-ray diffraction peak undergoes a shift as the specimen is tilted by an angle ψ , and the magnitude of the shift is related to the magnitude of the residual stress.

Table 1 Laser heating conditions used in the experiment

Scanning speed (cm/s) (mm/min)	Power (w)	Frequency (hz)	Nozzle gap (mm)	Nozzle diameter (mm)	Focus setting (mm)	N ₂ pressure (kpa)
10	80	1000	1.5	1.5	127	500

The relationship between the peak shift and the residual stress (σ) is [13] as follows:

$$\sigma = \frac{E}{(1 + \nu)\sin^2\psi} \frac{(d_n - d_o)}{d_o} \tag{1}$$

where E is Young's modulus, ν is Poisson's ratio, ψ is the tilt angle, and d_n are the d spacing of the diffraction peak measured at each tilt angle. In the absence of shear strains in the specimen, the d spacing changes linearly with $\sin^2\psi$, which is shown in Fig. 1. The calculations were performed for Cu₃N (100) planes ($2\theta=23.11^\circ$) with an interplane spacing of 0.3844 nm. It should be noted that Cu₃N is identified in accordance with the ICDD 00-055-0308 card. It can be observed that no shear strain developed in the specimen surface region and the residual stress is compressive. Figure 1 shows results in a slope of $-0.8 \times 10^{-3} \pm 9.12 \times 10^{-5}$ nm and intercept of $0.3844 \pm 4.75 \times 10^{-3}$ nm. The elastic module and Poisson's ratio of phosphor bronze are 96.5 GPa and 0.34 [14], respectively. The residual stress measured is on the order of -150 MPa, and the estimated error is ± 5 MPa, which is 3.3 %. It should be noted that the error is estimated based on three repeats of the XRD measurements.

2.2 Heating, thermal stress, and diffusion analysis

In the analysis, the solid body heat conduction with temperature-dependent conductivity, internal energy (including latent heat effects), and convection and radiation boundary conditions are considered. The Fourier heat transfer equation pertinent to the laser heat heating can be written as follows:

$$\rho \frac{\partial(CpT)}{\partial t} = (\nabla(k\nabla T)) + \rho U \frac{\partial(CpT)}{\partial x} + S_o \tag{2}$$

where k is the thermal conductivity, Cp is the specific heat capacity, ρ is the density, and S_o is the heat source term resembling the laser beam, i.e.:

$$S_o = I_o(1 - r_f)e^{(-\frac{x^2+y^2}{a^2})}e^{-\delta z} \tag{3}$$

Table 2 Elemental composition of bronze (in weight percent) used in the experiments

Cu	Sn	P
93.89	6.01	0.1

where I_o is the laser power peak density, a is the Gaussian parameter, r_f is the surface reflectivity, and x and y are the axes while the laser beam scans the surface along the x -axis with a constant velocity U . The laser beam axis is the z -axis (Fig. 2). It should be noted that the laser beam intensity distribution is assumed to be Gaussian at the irradiated surface.

Equation 1 is solved numerically with the appropriate boundary conditions to predict the temperature field in the substrate material. However, to analyze the phase change problem, the enthalpy method is used [15]. The specific heat capacity is associated with the internal energy gain of the substrate material, i.e., $Cp(T) = \frac{\partial U}{\partial T}$. However, the internal energy gain during the phase change is associated with the latent heat of fusion, which is given separately in terms of solidus and liquidus temperatures (the lower and upper temperature bounds of the phase change range) and the total internal energy associated with the phase change, called the latent heat [14]. To account for the forced convection cooling at the free surface during the gas-assisted nitriding process, the convective boundary with heat transfer coefficient of 3,000 W/m²K is considered at the free surface of the workpiece [16].

The elastic strain increment vector, $\{\Delta \epsilon^{el}\}$ is related to the stress increment vector, $\{\Delta \sigma\}$ by Hook's law:

$$\{\Delta \sigma\} = [D]\{\Delta \epsilon^{el}\} \tag{4}$$

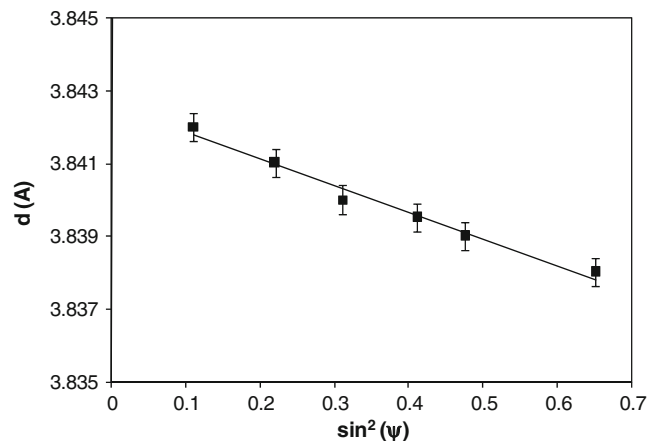


Fig. 1 Linear dependence of $d(100)$ on $\sin^2 \psi$

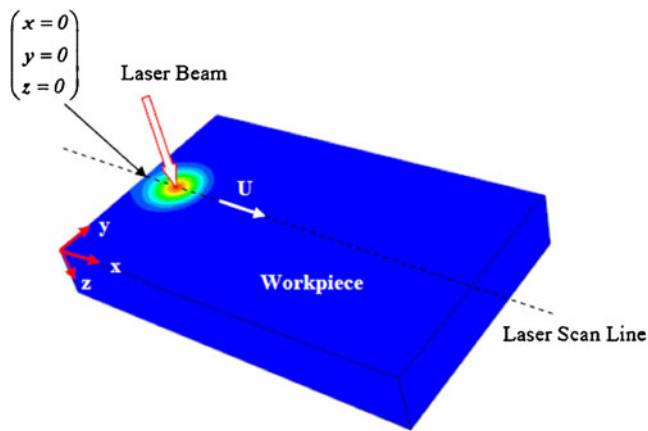


Fig. 2 Laser heating of the workpiece and the coordinate system

where $[D]$ contains the elastic constants related to temperature-dependent elastic modulus, E , and Poisson's ratio, ν . The total strain vector, $\{\Delta\varepsilon\}$, may be expressed as follows:

$$\{\Delta\varepsilon\} = \{\Delta\varepsilon^{el}\} + \{\Delta\varepsilon^{th}\} + \{\Delta\varepsilon^{pl}\} \quad (5)$$

where $\{\Delta\varepsilon^{el}\}$ is the elastic strain increment vector, $\{\Delta\varepsilon^{th}\}$ is the thermal strain increment vector, and $\{\Delta\varepsilon^{pl}\}$ is the plastic strain increment vector. The incremental thermal strain vector, $\{\Delta\varepsilon^{th}\}$, arises from the volume changes that accompany the temperature increment, ΔT , which is calculated by the thermal analysis. It is normally accounted for in stress analyses through a temperature-dependent differential thermal expansion coefficient, $\alpha(T)$. In the ABAQUS/Standard analysis, a spatially varying thermal expansion can be defined for homogeneous solid continuum elements by using a distribution, which includes the tabulated values for the thermal expansion [15]. The ABAQUS uses an implicit backward-difference scheme for time integration of both temperature and displacements at every material integration point [15].

2.3 Numerical simulation

Finite element discretization was carried out using the ABAQUS software [15]. The simulation is performed in the ABAQUS/Standard and consists of sequential thermal stress analysis. In the sequential thermal stress analysis, 91,572 elements are used to create the model using two element types; for the heat transfer analysis, mesh used elements of type DC3D4 (four-node linear heat transfer tetrahedron) and stress analysis used C3D4 (four-node linear 3D stress tetrahedron). The fixed boundary conditions are applied to the ends of the workpiece resembling the experimental laser heating situation. Table 3 gives the thermal properties of bronze used in the simulations.

In the stress analysis, displacements are stored by the ABAQUS at the nodal positions as a solution variable, and

Table 3 Thermal properties of bronze used in the simulations

Density (kg/m^3)	8,860
Latent heat of fusion (J/kg)	209,000
Solidus temperature (K)	1,227
Liquidus temperature (K)	1,367
Specific heat capacity (J/kgK)	377
Thermal conductivity (W/mK)	69.2

loads are defined as prescribed displacements and forces. Employing the interpolation functions, it is possible to calculate the strain and stress increments at any point within the element using the compatibility and constitutive equations. The ABAQUS transforms the mechanical equilibrium equations into a set of simultaneous equations, such that the nodal displacements and forces are related to each other through the elemental stiffness matrix. However, the ABAQUS uses a temperature-dependent total thermal strain coefficient, $\alpha'(T)$. The differential and total thermal expansion coefficients are related to each other through the following:

$$\alpha'(T) = \frac{1}{T - T^0} \int_{T^0}^T \alpha(T) dT \quad (6)$$

where T^0 is a reference temperature designating the point at which the material exhibits no dilatational strain (set to the mechanical coherency temperature in the current problem).

Laser heat flux with Gauss distribution and prescribed velocity of 10 cm/s along the x-axis through user subroutine DFLUX is applied to the thermal model. The Gauss parameter “ a ” is $a=0.00033$ m, in accordance with the experimental power intensity distribution. The thermal model consisted of two steps. The first step, which lasts 0.05 s, simulates the response of plate under moving laser heat flux. The second step, which lasts for 1,000 s, simulated the continued cooling in the model. Cooling was allowed to continue until all of the plate reaches initial temperature (room temperature). The temperature–time history resulted from the thermal analysis is used as input to the thermal stress analysis. The workpiece is considered as an elastic body, which is modeled as von Mises elastic-plastic material with isotropic hardening and with a yield stress that changes with temperature. Table 4 gives the properties of bronze used in the simulations.

The computational time and storage capacity required for simulating temperature and thermal stress fields are excessive due to the fine meshes used in the simulations. Therefore, the simulation time, which results in almost steady temperature and stress fields in the heated region is obtained through the initial simulation tests. The simulation corresponding to the heating time of 0.05 s results in almost

Table 4 Properties of bronze used in the simulations [14]

Temperature, K	Modulus of elasticity, E , pa	Poisson's ratio	Expansion coefficient, $1/K$
294	9.65E+010	0.34	1.54E-005
366	9.44E+010	0.34	1.58E-005
422	9.24E+010	0.34	1.62E-005
477	9.1E+010	0.34	1.66E-005
533	8.89E+010	0.34	1.73E-005
589	8.61E+010	0.34	1.77E-005
644	8.27E+010	0.34	1.81E-005
866	7.58E+010	0.34	2.0E-005
977	6.89E+010	0.34	2.1E-005
1088	4.82E+010	0.34	2.16E-005

steady temperature and stress predictions in the irradiated region. Consequently, the simulation is carried out once the steady-like temperature and stress fields are developed in the irradiated region. However, in the cooling cycle, temperature decays with progressing time and thermal stress fields vary accordingly. Therefore, the transient model is incorporated to capture temporal behavior of temperature and thermal stress fields. It should be noted that the laser scanning speed and the laser intensity distribution at the workpiece surface remain constant during the simulations, which are also true for the actual laser treatment process. This, in turn, results in steady-like processing in the irradiated region with progressing time.

3 Results and discussion

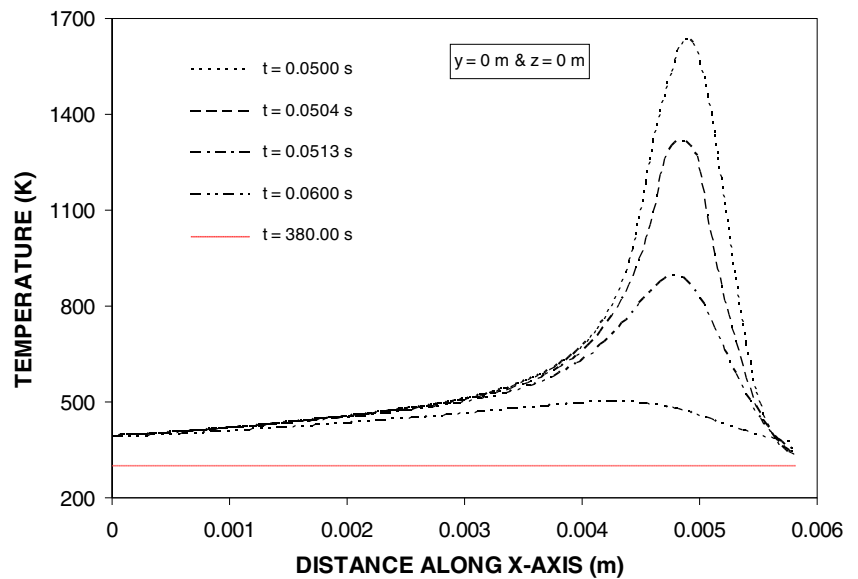
Laser surface treatment of bronze is carried out in nitrogen gas ambient condition. Thermal stress field and temperature variation in the irradiated regions are simulated using ABAQUS software [15] in line with the experimental parameters. The laser-treated surface is characterized using SEM, EDS, and XRD.

Figure 3 shows temperature distribution along the x -axis (laser scanning axis) for different cooling periods, while Fig. 4 shows temperature contours. It should be noted that $t=0.05$ s represents the initiation of the cooling period when laser power is switched off. In this case, the location of the laser beam axis is 0.005 m away from the start of laser scanning since the surface was scanned at a constant speed of 0.1 m/s. The maximum temperature is in the order of 1,700 K, which is higher than the melting temperature of bronze. The steady temperature region occurring during the phase change is not observable due to a small mushy zone generated around the melt pool. It should be noted that temperature remains the same in the mushy zone where both liquid and solid phases are present at the melting

temperature of the substrate material. Temperature increases gradually along the scanning line $0 \leq x \leq 0.004$ m. As the distance along the x -axis increases further, temperature rises sharply reaching its peak value. The gradual temperature rise along $0 \leq x \leq 0.004$ m is associated with the cooling of the surface initially heated by a laser beam during the scanning. Moreover, temperature decays sharply in the front region of the laser-irradiated spot ($0.005 \leq x \leq 0.006$ m). The sharp rise and decay of temperature around the irradiated spot result in high temperature gradient along the x -axis in this region. This enhances the heat diffusion from the heated region to the substrate material along the x -axis. This is more pronounced in the region ($0.005 \leq x \leq 0.006$ m) where the temperature decay is sharp. It should be noted that increasing temperature gradient enhances the heat diffusion from the irradiated region to the solid bulk [17]. As the cooling period progresses, temperature reduces sharply, i.e., it reduces to almost 900 K after $t=0.0013$ s from the initiation of the cooling period. This indicates that the cooling rate is considerably high. The sharp decay of temperature is attributed to the localized heating of laser spot, and heat transfer from the heated region to its neighborhood through conduction and convection is significant. As the cooling period progresses further, temperature reduces to initial temperature (which is 300 K) after 380 s.

Figure 5 shows von Mises stress distribution along the x -axis for the cooling periods similar to those shown in Fig. 3, while Fig. 6 shows von Mises stress contours. von Mises stress reduces significantly in the region of the irradiated spot immediately after the cooling cycle initiates ($0.05 \text{ s} \leq t \leq 0.0513 \text{ s}$). This is because of the temperature-dependent elastic modulus of the substrate material, which is incorporated in the simulations. In this case, elastic modulus reduces significantly with increasing temperature, and stress field reduces to

Fig. 3 Temperature variation along the x-axis for different cooling durations. The laser power ceases at $t=0.05$ s and $t=0.05$ s represents the initiation of cooling period ($z=0$ corresponds to the surface and $y=0$ is the laser scan line)



zero at the liquid state. However, as the cooling period progresses, temperature reduces (Fig. 3) and the von Mises stress attains significantly high values. This is true for $t \geq 0.06$ s. The attainment of high von Mises stress in the initially heated region along the x-axis ($0 \leq x \leq 0.003$ m) at the onset of cooling is because of the development of the thermal strain in this region, i.e., heat transfer from this region to the solid bulk lowers temperature while increasing the elastic modulus, and the temperature gradient developed along the x-axis in this region while enhancing von Mises stress. As the cooling period progresses further, temperature reduces significantly, and the stress field becomes the residual

stress. The high thermal strain developed along the x-axis is responsible for the formation of high residual stress levels after completion of the cooling cycle. von Mises stress reduces slightly in the region of $0.0052 \leq x \leq 0.0058$ m at the end of the cooling cycle. The reduction in von Mises stress is associated with the self-annealing effect; in which case, temperature is high (Fig. 3), resulting in the long cooling period at the location where the laser beam power ceases. Therefore, the slow cooling causes self-annealing while lowering the stress levels in this region. The maximum residual stress is in the order of 200 MPa, which is less than the elastic limit of the substrate material.

Fig. 4 Temperature contours in x, y-plane, and x, z-plane for the cooling period of $t=0.005$ s. The laser power ceases at $t=0.05$ s, and $t=0.05$ s represents the initiation of cooling period

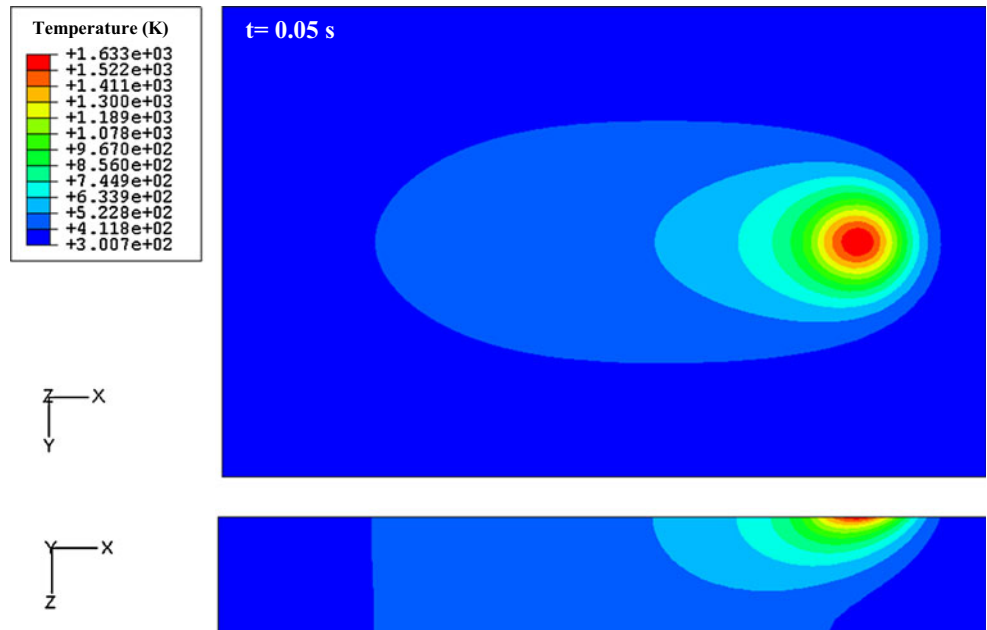


Fig. 5 von Mises stress variation along the x-axis for different cooling durations. The laser power ceases at $t=0.05$ s, and $t=0.05$ s represents the initiation of cooling period ($z=0$ corresponds to the surface and $y=0$ is the laser scan line)

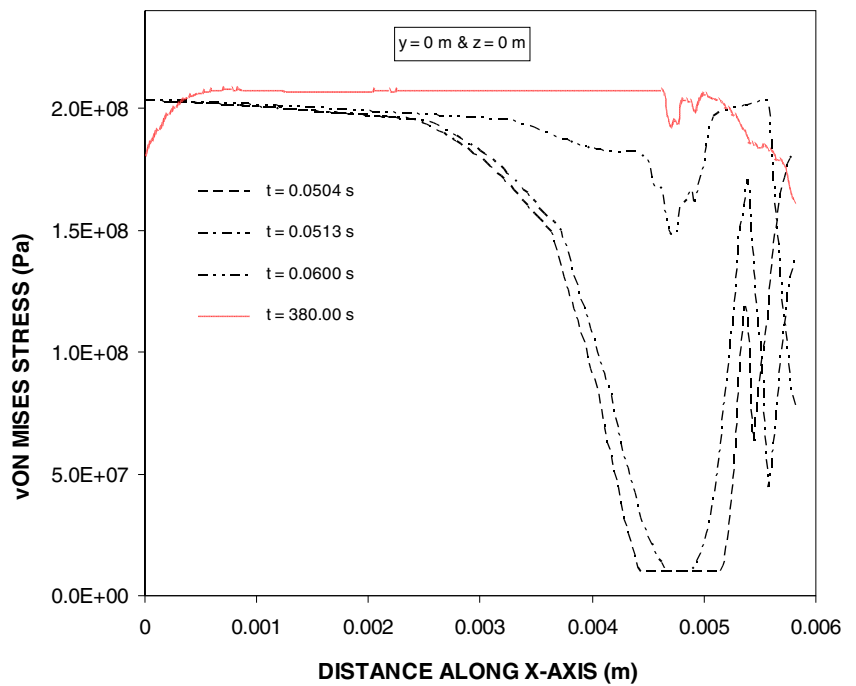


Figure 7 shows temperature distribution along the y-axis for different cooling periods, and x-axis is the location of the irradiated spot center at the surface. It should be noted that y-axis location $y=0$ corresponds to the center of the irradiated spot since $x=0.005$ m. Temperature rises sharply to reach maximum at the irradiated spot center. The presence of mushy zone where temperature remains at the melting temperature is not visible from the figures. This occurs because the size of the mushy zone is considerably small, and high

thermal conductivity of the substrate material contributes to narrow mushy zone formation. In the melt pool, temperature reaches well above the melting temperature of the substrate material; in which case, the superheating of liquid takes place. This enhances the melt pool size in both depth and width. This is more pronounced in the early cooling periods ($0.05 \text{ s} \leq t \leq 0.0513 \text{ s}$), i.e., the cooling rate is significantly high in the early periods. Moreover, as the cooling period progresses, the peak temperature reduces significantly, and temperature gradient also reduces around the heated spot.

Fig. 6 von Mises stress contours in x, y-plane, and x, z-plane for the cooling period of $t=0.05$ s. The laser power ceases at $t=0.05$ s, and $t=0.05$ s represents the initiation of cooling period

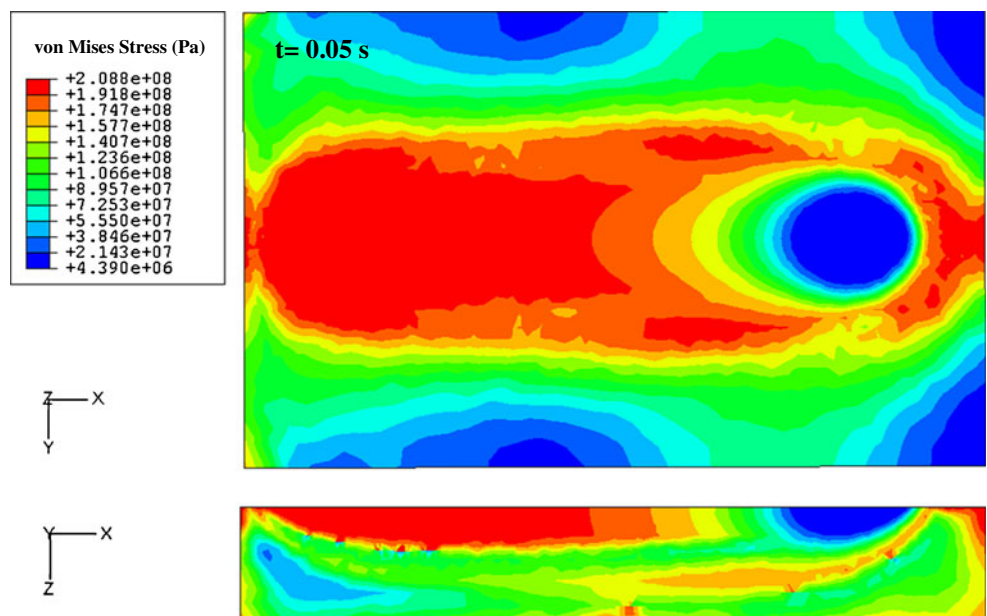
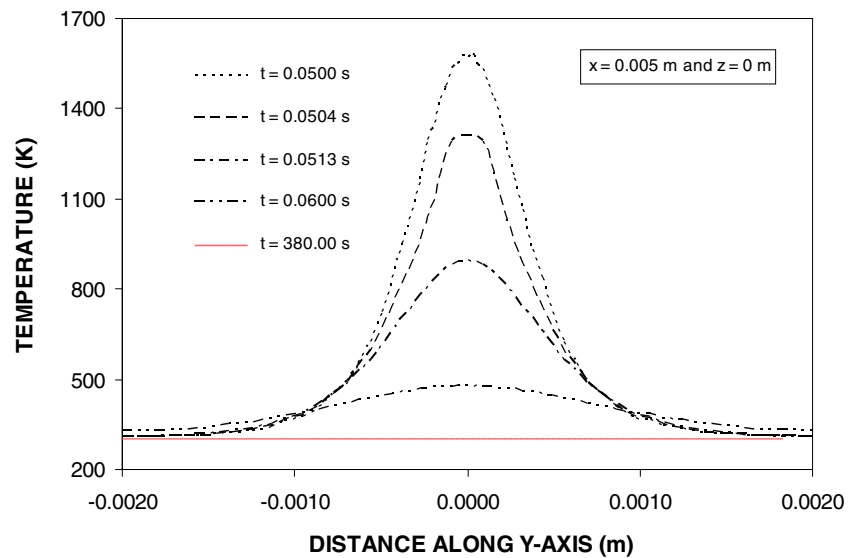


Fig. 7 Temperature variation along the y-axis for different cooling durations. The laser power ceases at $t=0.05$ s, and $t=0.05$ s represents the initiation of cooling period ($z=0$ corresponds to the surface, and $x=0.005$ m is the laser-heated spot center along the x-axis when cooling period initiates)



As the cooling period progresses further, temperature reduces to the initial temperature, and cooling cycle ends.

Figure 8 shows von Mises stress variation along the y-axis for different cooling periods, and x-axis location is $x=0.005$ m, which is the center of the irradiated spot. von Mises stress attains low values across the heated spot during the early heating periods. This behavior is associated with the attainment of the low values of elastic modulus at high temperatures as similar to the observation made in Fig. 5. As the cooling period progresses, von Mises stress attains high values because of increasing elastic modulus and the formation of high thermal strain across the heated spot. As the

cooling period progresses further, von Mises stress becomes the residual stress due to ending cooling period. The size of the high stress region extends beyond the heated spot size along the y-axis. This is attributed to the high temperature gradient developed around the heated spot edges, which, in turn, forms high thermal stains in this region.

Figure 9 shows temperature distribution inside the substrate material for different cooling periods, and x-axis location is $x=0.005$ m, which is the center of the irradiated spot. Temperature reduces sharply at the onset of cooling period. This results in high temperature gradient in the surface region, in particular, in the

Fig. 8 von Mises stress variation along the y-axis for different cooling durations. The laser power ceases at $t=0.05$ s, and $t=0.05$ s represents the initiation of cooling period ($z=0$ corresponds to the surface, and $x=0.005$ m is the laser-heated spot center along the x-axis when cooling period initiates)

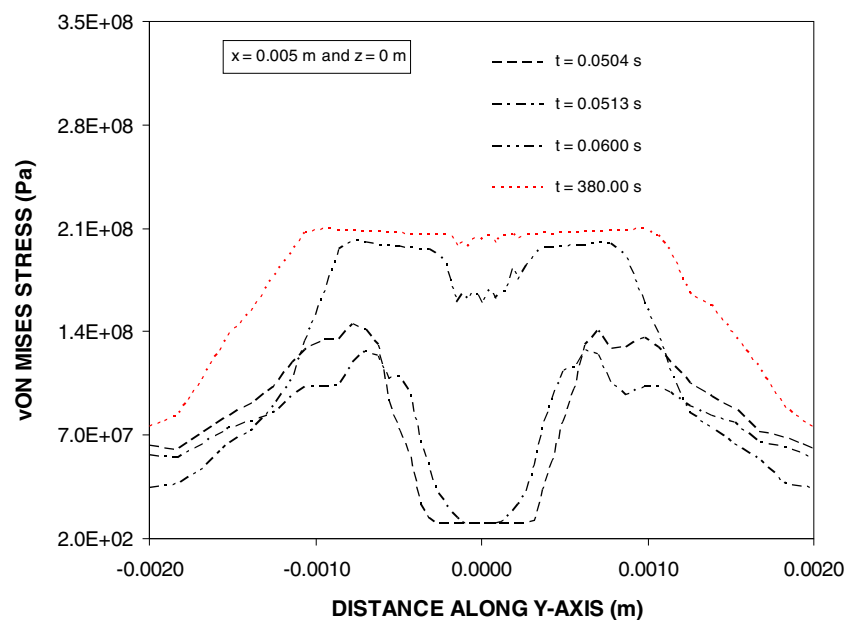
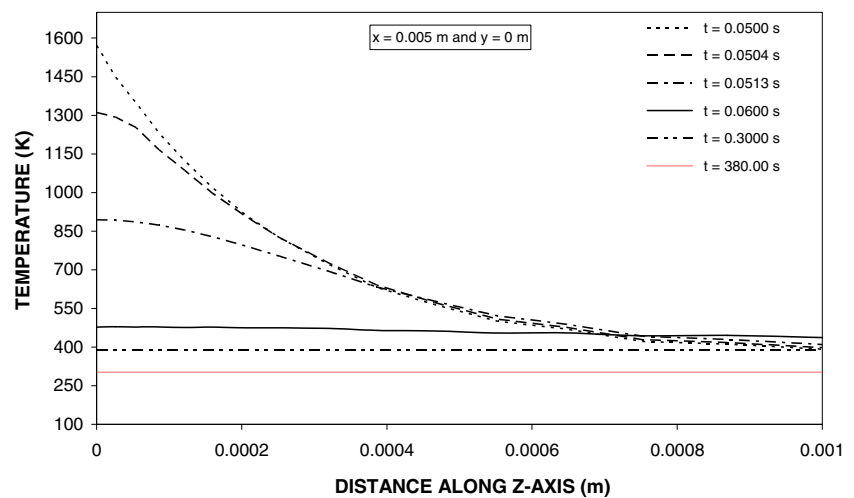


Fig. 9 Temperature variation along the z-axis for different cooling durations. The laser power ceases at $t=0.05$ s, and $t=0.05$ s represents the initiation of cooling period ($y=0$ corresponds to the laser scan line, and $x=0.005$ m is the laser-heated spot center along the x-axis when cooling period initiates)



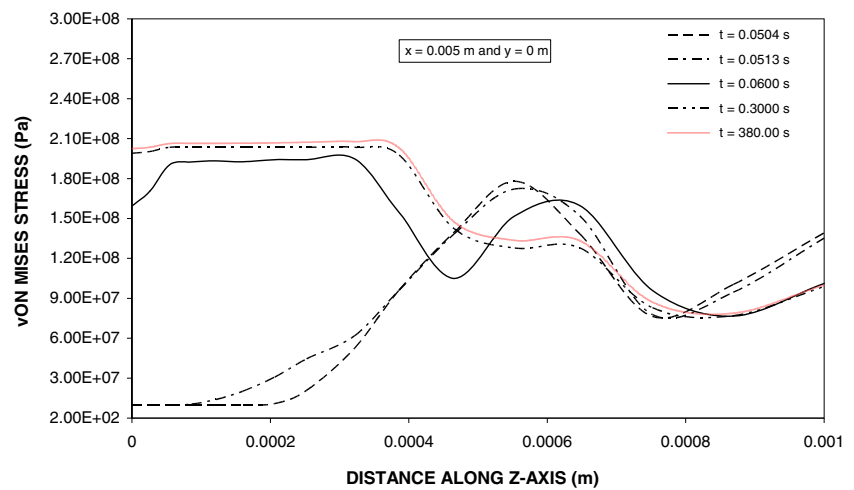
surface vicinity. This is attributed to the superheating of the liquid phase prior to the initiation of the cooling period and high thermal conductivity of the substrate material. However, when the cooling period progresses, temperature reduces gradually in the surface region and decreases sharply in the region next to the surface vicinity. This is because of the initially fast cooling of the superheated liquid in the irradiated region; in which case, temperature drops significantly in the irradiated region, and cooling rate slows down developing the low temperature gradient in the surface region. Consequently, the amount of the heat conduction in the surface vicinity ($0 \leq z \leq 0.00005$ m) becomes less. On the other hand, the temperature gradient is high in the region next to the surface vicinity. This accelerates the conduction loss from surface vicinity to the solid bulk while resulting in sharp decay of temperature in the region next to the surface vicinity.

Figure 10 shows von Mises stress distribution inside the substrate material for different cooling cycle periods, and x-axis location is $x=0.005$ m as similar to those shown in Fig. 9. von Mises stress is low in the surface region in the early cooling periods due to high temperature and low elastic modulus in the region. Moreover, von Mises stress attains high values in the surface region towards the end of the cooling period. The maximum von Mises stress is 200 MPa, which is less than the yielding limit of the substrate material. Moreover, the depth of high stress field extends 30–40 μm below the surface, and crack formation due to high stress field is unlikely. Figure 11 shows the residual stress predicted along the z-axis. It should be noted that at the end of the cooling cycle, temperature reduces to initial temperature and the stress field becomes residual stress in the substrate material. It is evident that the residual stress is compressive in the

surface region ($z < 0.00045$ m) and becomes tensile as the depth below the surface increases further. The magnitude of the residual stress at the surface vicinity ($z \leq 5 \mu\text{m}$) is on the order of -130 MPa. The maximum residual stress is -200 MPa, which occurs at z-axis location of 0.0003 m below the surface. However, the residual stress measured from the XRD technique is on the order of 150 MPa, which is in agreement with its counterpart predicted from the numerical simulations at the surface vicinity. It should be noted that the penetration depth for X-ray used in the experiment ($\text{CuK}\alpha$) is on the order of a few micrometers. Consequently, the comparison of the residual stress is made at the surface vicinity. Moreover, the difference between the experimental data and the prediction is due to assumptions made in the simulations and the error related to the measurements, which is on the order of 3.3 %.

Figure 12 shows optical photograph and SEM micrographs of laser-treated bronze surface. It is evident that laser tracks are formed due to laser scanning of the surface. The surface appears a mahogany; however, the presence of randomly scattered few red spots is an indication of copper. The mahogany color represents the presence of Cu_3N in the surface region. Moreover, the presence of copper indicates the dissolution of Cu_3N at elevated temperatures. Since the surface melts first and solidifies rapidly, the dissolution of Cu_3N does not cover the whole surface. The overlapping ratio of laser-scanned surface is over 80 %, which is evident from SEM micrograph. The roughness of the laser-treated surfaces is measured, and the averaged surface roughness is in the order of 3.6 μm , which is mainly associated with the overlapping of the melted spot, which was irradiated by a laser beam of a Gaussian intensity distribution. The close examination of the surface reveals that no cavity is formed due to surface

Fig. 10 von Mises stress variation along the z-axis for different cooling durations. The laser power ceases at $t=0.05$ s, and $t=0.05$ s represents the initiation of cooling period ($y=0$ corresponds to the laser scan line, and $x=0.005$ m is the laser-heated spot center along the x-axis when cooling period initiates)



evaporation, and no cracks are observed at the surface. The close examination of surface reveals that submicron grains are formed during the nitriding process. This is because of the rapid solidification and formation of nitrides in the surface region. Although Cu_3N grains are small, the submicron size of the packed particles suggests that each particle contains many single crystals of Cu_3N . The similar observation was also reported in the early study [9]. Moreover, no submicron cracks between the packed grains are observed due to thermal stress developed in this region. Some small fine grains at nanosizes are also evident; this is the indication of the presence of Cu_3N compound in the surface region.

Figure 13 shows SEM micrographs of a cross section of laser-nitrided region. It is evident that almost uniform

laser-treated layer is formed, and the depth of the treated layer extends almost $50 \mu\text{m}$ below the surface. The close view of the SEM micrographs in the surface region reveals that a dense structure is formed at the surface. The submicron-sized packed particles and extremely fine grains are evident in the surface region. The packed particles are closely situated particularly in the surface region. Table 5 gives the EDS data and SEM micrograph showing the locations of the EDS spectrums. It is evident that the nitrogen concentration is high in the surface region. However, the nitrogen concentration is zero at $30 \mu\text{m}$ below the surface (spectrum 3). This reveals that the nitrogen diffusion is shallow and smaller than the laser-treated zone. Moreover, the absence of Sn in the spectra 1 and 2, which are located in the surface region, indicates that Sn evaporates in the surface region during the laser treatment process. Since the amount of Sn in the alloy is about 6 %, the cavity formation at the surface due to the evaporation is not observed. The heat-affected zone is narrow, and there is no clear demarcation line between the heat-affected zone and the base material. This is attributed to the high thermal conductivity of the bronze, which results in low temperature gradient in this region. Figure 14 shows XRD diffractogram after the laser treatment process. The presence of Cu_3N (100) is evident, which is associated with the high nitrogen pressure during incorporation in the laser treatment process. The similar observation was reported for Cu_3N films formed on the silica glass during magnetron sputtering [9]. The presence of copper peak reveals the dissolution of Cu_3N in the cooling period. The microhardness of the laser-treated surface is high (580 ± 20 HV), which is almost four times the hardness of the base material (145 ± 15 HV). This is due to the following: (a) the dense structure formed in the surface

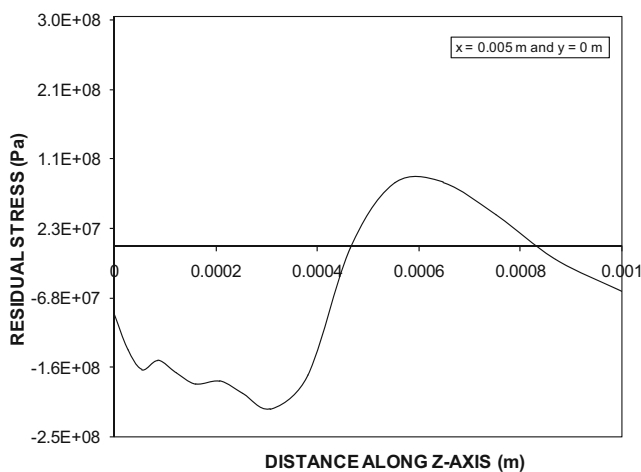
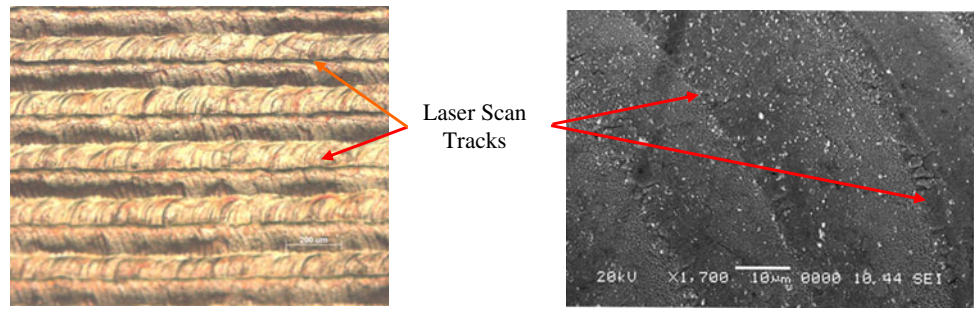


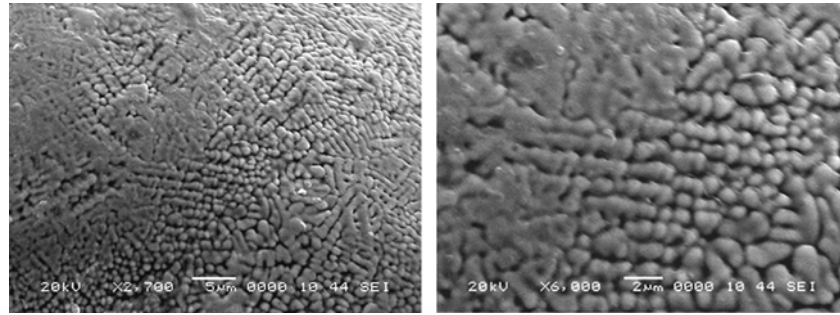
Fig. 11 Residual stress predicted along the z-axis at the end of the cooling period ($y=0$ corresponds to the laser scan line, and $x=0.005$ m is the laser-heated spot center along the x-axis when cooling period initiates)

Fig. 12 Optical photograph (upper left) and SEM micrograph of laser-treated surface (upper right) and close view (lower left and lower right)



Optical photograph of laser treated surface.

SEM Micrograph of laser treated surface.

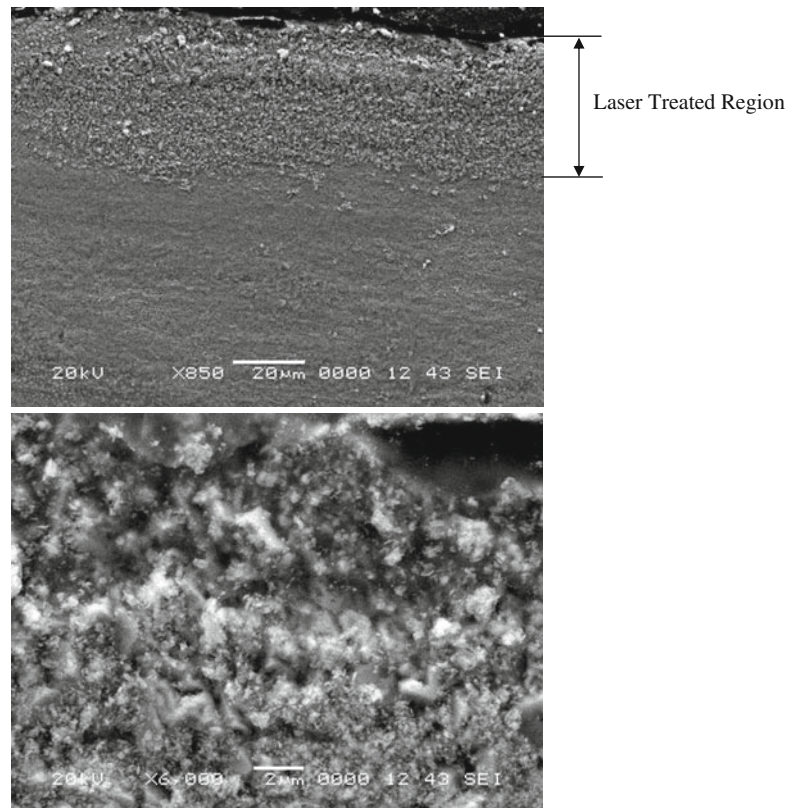


SEM micrograph of laser treated surface (close view).

region and (b) the formation of Cu_3N compounds in the surface region after the laser treatment process. Since

the depth of the laser-treated layer extends $50\ \mu\text{m}$ below, the hardness variation along the depth of the

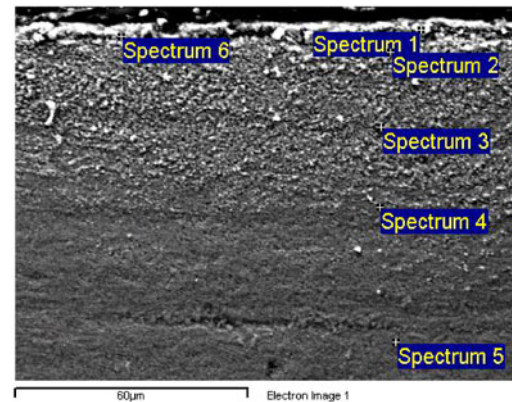
Fig. 13 SEM micrographs of the cross section of the laser-treated workpiece. Fine and dense structures in the surface vicinity of the laser-treated workpiece are shown



Fine and dense structures in the surface vicinity of the laser treated workpiece.

Table 5 EDS data obtained in the laser-treated region and locations of spectrums

Spectrum	C	N	O	Sn	Cu
Spectrum 1	7.97	19.74	24.40	0.00	Balance
Spectrum 2	2.15	21.63	24.11	0.00	Balance
Spectrum 3	0.00	0.00	2.13	4.49	Balance
Spectrum 4	0.00	0.00	0.00	6.01	Balance
Spectrum 5	0.00	0.00	4.03	5.97	Balance
Spectrum 6	23.03	38.36	33.00	0.00	Balance

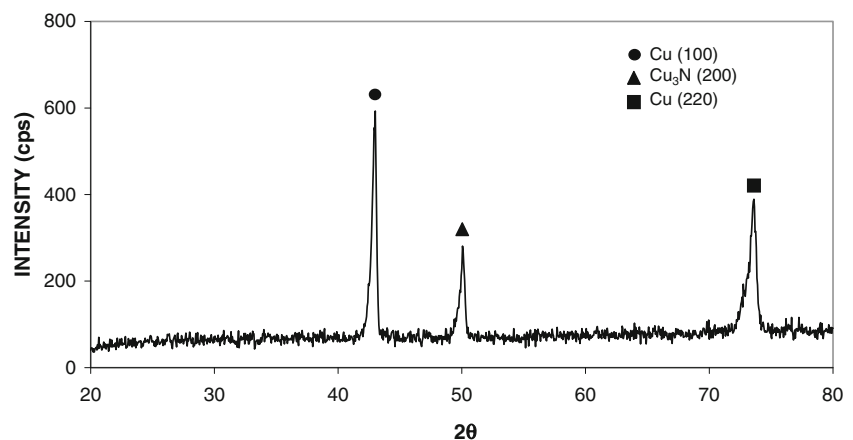


treated layer is difficult to obtain with accuracy using the microindenter, and it requires the nanoindenter for the accuracy; therefore, it is left for the future study.

4 Conclusion

Laser treatment of bronze surface is carried out. Temperature and stress fields are modeled in three-dimensional space and computed in line with the experimental conditions. Microstructural and morphological changes in the laser-treated region are examined using SEM, EDS, and XRD. It is evident that superheating of liquids occurs in the melt pool, which influences the temperature gradient in the surface region onset of the cooling cycle initiation. This is more pronounced along the z-axis. von Mises stress attains low values during the early period of cooling cycle, which is associated with the low elastic modulus at high temperatures. However, as the cooling period progresses further, temperature reduces to initial temperature, and von Mises stress becomes the residual stress. The high residual stress region extends beyond the region covered by the irradiated spot. This is attributed to high thermal stain developed in the

vicinity of the irradiated spot circumference. Moreover, the residual stress remains high in the surface region (30–40 µm below the depth). The maximum residual stress is in the order of –200 MPa, which is less than the elastic limit of the substrate material. Laser-treated surface is smooth and free from cracks, voids, and cavities. The dense structure consisting of fine grains are formed in the surface region of the laser-treated workpiece. The cross-sectional examination of the laser-treated region shows that the dense structure formed in the surface region is free from cracks, which is attributed to residual stress levels, which is less than the yielding limit of the substrate material. The XRD diffractogram reveals that Cu_3N compound is formed in the surface region. However, the presence of locally scattered few large copper grains indicates the dissolution of Cu_3N into copper and N_2 during the early cooling period. The uniform thickness of nitrided layer in the surface region indicates the uniform heating of the surface during the laser scanning at a constant speed. The microhardness of the surface increases almost four times of the base material hardness. This occurs because of the dense structure and nitride compound formed in the surface region.

Fig. 14 XRD diffractogram of laser-treated surface

Acknowledgments The authors acknowledge the support of King Fahd University of Petroleum and Minerals, Dhahran, Saudi Arabia for supporting the funded project # SB111003.

References

- Vanderberg JM, Draper CW (1984) An X-ray diffraction study on the microstructure of laser surface melted Cu–Al–Fe alloys. *Materials Letters* 2:386–392
- Gabriel MW, Preece CM, Staudinger A, Draper CW (1981) Cavitation erosion of laser quenched Fe–aluminum bronze. *IEEE J Quantum Electronics* QE-17:2000–2003
- Maruyama T, Morishita T (1996) Copper nitride and tin nitride films for write-once optical recording media. *Appl Phys Lett* 69:890–891
- Zukowski P, Karwat C, Komarov FF, Komarov AF, Latuszynski A (1996) Formation of copper nitrides in the course of implanting copper with large doses of nitrogen ions. *Phys Stat Sol A* 157:373–378
- Wang J, Chen JT, Yuan XM, Wu ZG, Miao BB, Yan PX (2006) Copper nitride (Cu₃N) thin films deposited by RF magnetron sputtering. *J Crystal Growth* 286:407–412
- Pierson JF (2002) Structure and properties of copper nitride films formed by reactive magnetron sputtering. *Vacuum* 66:59–64
- Borsa DM, Boerma DO (2004) Growth, structural and optical properties of Cu₃N films. *Surface Science* 548:95–105
- Tang CH, Cheng FT, Man HC (2004) Improvement in cavitation erosion resistance of a copper-based propeller alloy by laser surface melting. *Surface and Coatings Technology* 182:300–307
- Yue GH, Yan PX, Wang J (2005) Study on the preparation and properties of copper nitride thin films. *J Crystal Growth* 274:464–468
- Ciristina LJ, Vidal RA, Ferron J (2008) Surface characterization of nitride structures on Cu(001) formed by implantation of N ions: an AES, XPS and LEIS study. *Surface Science* 602:3454–3458
- Yilbas BS, Arif AFM, Karatas C, Akhtar S, Abdul Aleem BJ (2010) Laser nitriding of tool steel: thermal stress analysis. *Int J of Advanced Manufacturing Technology* 49:1009–1018
- Buena Park, CA (877) AMADA-US 7025 Firestone Blvd. Buena Park, CA 90621.
- Khana ZA, Hadfield M, Tobe S, Wang Y (2005) Ceramic rolling elements with ring crack defects—a residual stress approach. *Materials Science and Engineering A* 404:221–226
- Young Modulus of Elasticity for Metals and Alloys & Coefficients of Linear Expansion: <http://www.engineeringtoolbox.com/>
- ABAQUS Inc (2001) ABAQUS Theory Manual, Version 6.2, ABAQUS Inc., Pawtucket, USA.
- Shuja SZ, Yilbas BS (2000) The influence of gas jet velocity in laser heating-a moving workpiece case, *Proc Instn Mech Engrs. Part C J Mechanical Engineering Science* 214:1059–1078
- Yilbas BS, Shuja SZ (1997) Heat transfer analysis for surfaces—conduction limited case. *Applied Surface Science* 108:167–175